

Double-Helix Active Geometry: LiDAR-Anchored Multi-View Depth with Selective Abstention

Jinwen Wen
Independent Researcher

July 7, 2026

Abstract

Consumer depth sensors such as the LiDAR scanner on recent iPhones provide metric range, but their useful range is short and their returns are sparse. We present **DH-Active**, a lightweight, training-free geometry back-end that treats the sensor as a *metric ruler* rather than the sole source of depth. Near-field returns anchor the metric relative pose of two views through PnP; visually trackable samples without a valid depth return are then triangulated under that pose. A parallax/reprojection gate abstains wherever the geometry is ill-conditioned, leaving an explicit hole and a selective score instead of forcing an estimate. The measured core front end—spiral sampling, sparse back-projection, and hole taxonomy, excluding preprocessing and multi-view recovery—runs at **1.11 ms** median latency on CPU (OpenCV using 14 threads), about 38× faster than a DINOv2-L visual branch on GPU in our timing setup. Across two iPhone captures and the public TUM RGB-D and ARKitScenes benchmarks, held-out depth is recovered at 1.4–6.7% median relative error. In a controlled ARKitScenes protocol that uses only returns within 2 m to set scale and an independent laser scan as ground truth, DH-Active achieves **64.2% scene-median coverage** of evaluable far-field candidates at **13.4% scene-median relative error**; direct triangulation from the device trajectory is not usable. We also report the alternatives that failed in our tests: single-frame defocus, classical focus-stack depth, defocus–LiDAR fusion, point-to-point ICP over a good visual-inertial track, and attention-to-holes resampling. A 1.26 B learned model remains more accurate after oracle scale alignment. The contribution here is narrower: metric sparse depth, explicit abstention, zero learned parameters, and near-millisecond CPU cost.

1 Introduction

A robot or embodied agent that wants to act in a room needs to know where surfaces are, in metres, and—just as importantly—needs to know *where it does not know*. Active depth sensors such as the LiDAR scanner on recent iPhones are metric and robust, but their usable range is short: distant, reflective, or grazing surfaces often receive no return. Learned depth completion and multi-view systems can fill gaps, but they require training and usually a GPU for practical throughput. Large visual encoders used in vision–language–action (VLA) systems [13, 18] provide powerful image features, not by themselves metric depth. This leaves room for a small geometric back-end that uses the metric signal already on the device and reports when it has too little evidence.

This paper asks a narrow, deployable question: *on a device that already carries a short-range metric sensor, how far can purely geometric reasoning extend that sensor, without any learning, while remaining honest about its own failures?* Our answer is a system, DH-Active, organised around a single principle:

*Demote the strong-but-short-range active sensor from the only depth source to a **metric ruler**: use its near returns to fix the metric relative pose between views, use that pose to triangulate the far field it cannot itself reach, leave an explicit hole where neither can see, and attach a selective confidence to every estimate.*

Concretely, DH-Active samples each frame along a pair of foveated spiral trajectories [21, 26], back-projects the near LiDAR returns at those samples into a confidence-tagged sparse 3D set, and classifies every *missing* sample by why it is missing. For samples that lack a valid depth return but remain visually trackable, it estimates the metric two-view relative pose by solving Perspective-n-Point [7, 14] on the near points that *do* have depth, then triangulates the far points under that pose. A parallax and reprojection gate discards ill-conditioned rays, so the system reports “could not recover” rather than a confident guess—a deliberate design choice in the spirit of selective prediction [5, 8].

We stress at the outset what this work is and is not. It is *not* a new state of the art in depth accuracy: a 1.26 B-parameter learned multi-view model is markedly more accurate, albeit only up to scale and only on a GPU (§6.6). It *is* a study of how much honest, metric geometry one can extract on commodity hardware at near-zero cost, and of where that approach breaks. The word “active” in the name refers to the active depth input and the foveated-sampling line of work from which the project grew. The evaluated system does not plan camera motion or choose robot actions. Our contributions are:

1. **A LiDAR-as-ruler far-field depth pipeline.** A self-consistent loop in which the same near-field returns supply both metric depth and the pose scale needed to triangulate the far field, recovering points genuinely beyond sensor range, with no network and no training (§3).
2. **Abstention as a first-class output.** A parallax/reprojection gate and a per-point selective score that trade coverage for tail-risk; we show on a strict near/far protocol that the gate, not the resampling, is the core safety mechanism (§6.4, 6.5).
3. **A controlled-cutoff evaluation with independent ground truth** that directly measures far-field recovery on a fixed evaluable cohort: all returns beyond 2 m are masked and the outputs are scored against a static laser scan (§6.4).
4. **A documented set of negative results**—defocus depth, focus stacks, defocus–LiDAR fusion, ICP over a good visual-inertial track, and attention-to-holes—tested with explicit controls (§4). These delimit where the simple geometry is and is not the right tool, and are, we argue, as useful as the positive results.
5. **An efficiency characterisation** against a DINOv2-L visual branch on the same machine: $\sim 38\times$ lower measured latency for the core CPU front end versus the encoder on a GPU, at zero learned parameters (§6.1), plus a descriptive downstream comparison (§6.7).

2 Related Work

Structure from motion and SLAM. Recovering pose and structure from multiple views is classical [10]. Modern pipelines—COLMAP for offline reconstruction [20], ORB-SLAM3 for real-time tracking [2]—estimate camera motion and a (typically dense or semi-dense) map jointly. Metric scale comes from cues such as calibrated stereo, RGB-D, or inertial measurements; loop closure corrects drift but does not itself supply absolute scale. DH-Active deliberately occupies a smaller niche: it does not build or optimise a global map, performs no bundle adjustment or loop closure, and instead uses an already-present metric sensor to fix two-view scale locally. Where RGB-D fusion methods such as KinectFusion [17] integrate *dense* depth into a volumetric field [4], our measurements are sparse spiral samples and our emphasis is on the points the depth sensor *misses*.

Sparse depth completion. RGB-D completion commonly densifies a sparse or incomplete depth map with learned image priors [30, 31]. Recent systems also combine sparse direct time-of-flight returns with dense image features [12] or use LiDAR to prompt spatio-temporal multi-view stereo [25]. These methods target dense prediction and generally rely on learned components, supplied poses, or both. DH-Active makes a different trade: it produces only sparse metric estimates, learns no image prior, estimates the two-view metric pose from the near returns themselves, and abstains when the recovered ray geometry is weak.

Pose from known-depth points. Solving for camera pose from 2D–3D correspondences is the Perspective-n-Point problem [14], robustified with RANSAC [7]. Using LiDAR-backed points to anchor metric pose, and short Lucas–Kanade [15] tracks of Shi–Tomasi features [22] to form correspondences, are individually standard. Our contribution is not a new estimator but the *closed loop*: the near returns that the sensor provides for free are exactly what make the far-field triangulation metric, and we show that substituting the device’s own visual-inertial pose for this PnP step collapses the result (§6.4).

Learned multi-view geometry. Recent transformers regress geometry directly from images: DUST3R aligns image pairs into a common point map [29], and VGGT predicts cameras, depth, and point maps feed-forward [28]. These are accurate but output structure *up to scale*, carry hundreds of millions to billions of parameters, and are normally run on a GPU for practical throughput. We use them as reference points (§6.6); the largest is more accurate after scale alignment, whereas DH-Active obtains metric scale from the sensor rather than a ground-truth fit.

the reprojection residual is below 3 px. Endpoints may use distinct intrinsics ($K_{\text{anchor}} \neq K_{\text{current}}$), which we verify with a synthetic regression test. The gate is the system’s reject option: it is what turns an over-confident far-field guess into an explicit, reported hole.

3.4 Selective confidence

Each surviving point carries a continuous score derived from its parallax and reprojection residual. Sweeping a threshold over this score induces a risk–coverage curve, and we use it as a *selective* signal. Higher thresholds keep fewer points and initially reduce error, but the trend is not strictly monotone. We show in §6.3 and §6.4 that the score provides a useful ordering while its expected calibration error remains too high to call it a calibrated probability; we therefore avoid that word throughout.

3.5 Global integration (scope note)

Recovered points can be fused into a confidence-weighted truncated signed-distance field [4, 17] for visualisation, with overlap regions blended by confidence rather than overwritten. This widens map coverage but, as we report honestly in §7, does *not* stitch the sparse single-view fragments into a closed room; global mapping is outside the scope of the claims we defend here.

4 What Does Not Work

The design above is the residue of a sequence of alternatives that did not survive their screening tests. Most use the in-house captures; the focus-stack study instead uses the public synthetic FoD500 set [16] and real DDF-12 light-field data [11]. We report these results because they delimit where simple geometry is the wrong tool and explain why the final system relies on the ruler-and-gate loop.

- **Dual-helix temporal cross-correlation.** The project’s original intuition—that two phase-shifted 1D spiral signals could be cross-correlated to “squeeze out” parallax—is *false*. Against LiDAR inverse depth it scores $r = -0.04$, versus $+0.34$ for plain 2D optical flow: under forward motion the flow is radial and a 1D tangential correlation is structurally blind to it.
- **Single-frame depth from defocus.** The defocus signal is real but weak ($|\rho|$ median 0.22) and dominated by two ambiguities: texture (a blank wall looks defocused) and sign (near vs. far of focus). A sign-only oracle reaches $r = 0.66$, but a deployable single-frame estimator that must *produce* the sign collapses to $r = 0.06$.
- **Classical focus-stack depth.** On clean synthetic data argmax-sharpness reaches Spearman 0.69 (gated Pearson 0.76), but on real light-field data it swings with the scene, flips sign on $\sim 1/5$ of scenes, and confidence gating cannot rescue it (it is “confidently wrong”): top-25% $|r|$ rises only $0.15 \rightarrow 0.21$.
- **Defocus–LiDAR fusion for densification.** On this hardware plain bilinear upsampling of LiDAR already reaches $r \approx 0.82\text{--}0.99$; defocus guidance never beats it and slightly *raises* error. The sensor is too clean to leave defocus any detail to add.
- **Point-to-point ICP over a good VIO track.** With a reliable device pose, ICP between two independently resampled sparse sets is ill-posed and rarely confident; trusting VIO alone covers *more* (6,200 vs. 5,417 voxels) than applying ICP. ICP earns its keep only when no reliable pose exists. This is the same lesson as defocus-vs-LiDAR: a strong prior makes the clever add-on redundant.
- **Attention-to-holes resampling.** Moving the foveal centre onto the largest hole cluster makes coverage *worse* (hole rate $0.67 \rightarrow 0.78$): the holes here are sensor missing-depth regions rather than a shortage of sample locations, so resampling cannot create a return the sensor never gave. This result supports using the active layer for *routing* (“this may need a head turn, not an eye movement”) rather than claiming that it fills depth.

5 Experimental Setup

Data. We use two in-house iPhone captures via Record3D (one indoor, near-static hand-held; one outdoor, walking), and public datasets for the positive and negative studies: **TUM RGB-D** (11 sequences, structured-light depth) [24]; **ARKitScenes** (Apple-LiDAR RGB-D with a registered high-resolution laser scan) [1]; and **RH20T** (real RGB-D with robot action labels) [6]. The focal-stack screening uses **FoD500** (500 synthetic five-image stacks) [16] and **DDFF-12** (real refocused light-field stacks from 12 scenes) [11]. Public datasets are obtained from their official sources; no data or model weights are redistributed.

Protocol. Our central metric is the relative error of recovered metric depth against a reference, reported as a per-sequence median and then a scene-median over sequences (to keep long videos from dominating), alongside the 90th percentile (p90) as a tail-risk measure, Pearson correlation, and *coverage* (fraction of evaluable candidates the method chooses to output). Reporting coverage beside accuracy is essential for a method that abstains. Unless noted, depth hold-outs split points so that pose calibration and evaluation never share a point.

Reproducibility. The geometry runtime has no deep-learning dependencies; 72 offline unit tests cover the pipeline. Each experiment archives a JSON of its full configuration and per-sequence numbers. Baseline encoders (DINOv2, DUST3R, VGGT) use official code and checkpoints fetched separately and are timed/scored as-is.

6 Results

6.1 Deployment efficiency

We time the core DH-Active front-end stages against the DINOv2-L visual branch of a VLA encoder on the same Apple M4 Pro (batch 1, fp32, warm-up, $p_{50}/p_{95}/p_{99}$; DINOv2 uses randomly initialised weights because the forward cost is unchanged). This is an explicitly scoped cost comparison, not a claim that the two branches compute the same function.

Table 1: Measured front-end latency at 224×224 . DINOv2 numbers are encoder forward passes; DH-Active covers spiral sampling, sparse back-projection, and hole taxonomy.

Branch	device	p_{50} (ms)	learned params	weight size / GPU peak
DINOv2-L	CPU	106.5	303 M	1.2 GB
DINOv2-L	GPU (MPS)	42.0	303 M	2.2 GB peak
DH-Active core front end	CPU	1.11	0	0 / n.a.

The measured core front end runs in 1.11 ms (p_{95} 1.24, p_{99} 1.34) with OpenCV configured for 14 CPU threads: $96\times$ lower latency than DINOv2-L on CPU and $38\times$ lower than its MPS run in this setup, with no learned parameters or weight storage (Fig. 2). The timing excludes image/depth preprocessing, feature tracking, PnP, and triangulation and therefore is not an end-to-end pipeline number. At 1440×1920 the same measured stages take 3.81 ms. The comparison concerns cost rather than function: DINOv2 emits dense visual features, while DH-Active emits sparse RGB-D geometry metadata.

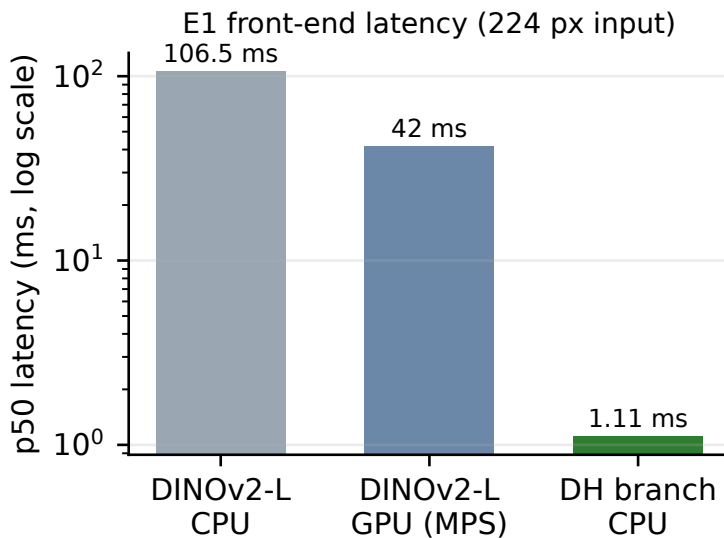


Figure 2: Measured front-end latency (log scale). The DH-Active core stages are near-millisecond on CPU; DINOv2-L is timed as an encoder forward pass.

6.2 Held-out triangulation on in-house captures

On each iPhone capture we split LiDAR-backed trackable points so that PnP pose calibration (set A) and evaluation (set B) are disjoint, and triangulate B under the A-calibrated pose. A naive “cyclic” protocol, which evaluates on the very inliers RANSAC optimised, reports 0.7% error; the honest hold-out is 5× worse, underscoring why the split matters.

Table 2: Hold-out triangulation on in-house captures (set B never sees pose calibration). Camera motion is the dominant factor.

Capture	hold-out pts	corr	median rel. err.	reproj.
indoor (near-static)	225	0.963	3.5%	0.96 px
outdoor (walking)	2,010	0.974	1.4%	0.74 px

Both pass the strict criterion (corr > 0.8, rel < 10%, reproj < 3px). The walking capture recovers 663 hole candidates versus 105 indoors (about 6×) and is more accurate, consistent with the method’s dependence on translational baseline. Recovered hole candidates in that capture extend to 6.1 m, beyond the useful range observed from the device sensor. When parallax is small, the gate responds by returning fewer points.

6.3 Cross-dataset geometry and calibration

We validate the depth-anchored geometry across scenes on two public benchmarks. On TUM RGB-D (11 sequences) the scene-median relative error is **2.6%** (per-sequence 1.0–4.2%), correlation 0.806, with 8/11 passing the strict line. On ARKitScenes (5 Apple-LiDAR sequences, the closest public analogue to our own hardware) the scene-median relative error is **6.7%** but correlation drops to 0.745 and only 1/5 passes the strict line—handheld fast motion and 256×192 depth make the public set materially harder. Two honest caveats apply throughout: (i) TUM depth is structured-light, so it validates the geometry, not iPhone-LiDAR generalisation; and (ii) the medians are computed over points the gate *keeps*, so low error co-occurs with low coverage (as low as 1% of candidates on a large-rotation sequence). We make this selection effect explicit rather than hiding it, and the controlled protocol of §6.4 fixes the evaluable cohort so that the effect can be measured rather than hidden. The gate still selects which candidates receive an output.

Calibration. Binning recovered points by confidence and comparing to actual error shows that the score generally orders points by risk but is materially miscalibrated. Reliability bins include both under- and over-confident regions across sequences, with a median expected calibration error (ECE) of 0.284 on TUM and 0.224 on ARKitScenes. An ECE this large is why we report the score as selective, not calibrated; temperature or isotonic recalibration is left as future work.

Table 3: Cross-dataset depth-anchored geometry. Coverage is the fraction of candidates kept; its variability is the selection effect that §6.4 measures on a fixed cohort.

Benchmark	seqs	median rel. err.	corr	ECE (med.)
in-house iPhone	2	1.4–3.5%	0.96–0.97	—
TUM RGB-D [24]	11	2.6%	0.806	0.284
ARKitScenes [1]	5	6.7%	0.745	0.224

6.4 Strict near/far range split (controlled far-field recovery)

The hold-outs above mix near and far points. To test the core claim directly—*can near-field returns alone recover true far-field depth?*—we run a controlled protocol on five ARKitScenes sequences. We mask every LiDAR return beyond a cutoff (default 2 m), allow PnP to use *only* the near points, and score recovered far-field depth against the registered high-resolution *laser* scan, which is independent of the low-res LiDAR. Ground truth is quality-controlled (nearest-neighbour aligned, ≤ 80 ms temporal gap; accepted high-res anchors agree with low-res returns to 1.3% where both exist).

Table 4: Controlled far-field recovery on ARKitScenes, cutoff = 2 m, range-masked cohort (32,690 pooled candidates). Entries are scene medians over five sequences. Triangulation from the device trajectory is not usable; LiDAR-anchored PnP recovers a majority of evaluable candidates.

method	coverage	corr	median rel.	p90 rel.
sensor-only (after cutoff)	0.0%	—	—	—
device pose (raw)	0.4%	-0.33	126.0%	663%
device pose (GL→CV)	3.5%	-0.44	57.3%	375%
DH-Active, no gates	68.0%	0.02	14.1%	41.0%
DH-Active, gated	64.2%	0.26	13.4%	35.6%

DH-Active reaches **64.2%** scene-median coverage of evaluable far-field candidates at **13.4%** scene-median relative error. Across individual sequences, coverage spans 47.7–88.8% and median relative error 8.5–14.1%. The pooled output count is 22,045 of 32,690 candidates (67.4%); we report scene medians in the table so that the longest sequence does not dominate. Direct use of the device trajectory yields very few, highly inaccurate outputs, showing that the LiDAR-anchored PnP step—not triangulation alone—provides usable metric geometry in this test. The gate lowers the scene-median tail (p90 41.0→35.6%) at a small coverage cost, while still selecting which candidates receive an output. At confidence 0.3, median error falls to 9.5% at 34.3% coverage; stricter thresholds no longer improve error monotonically.

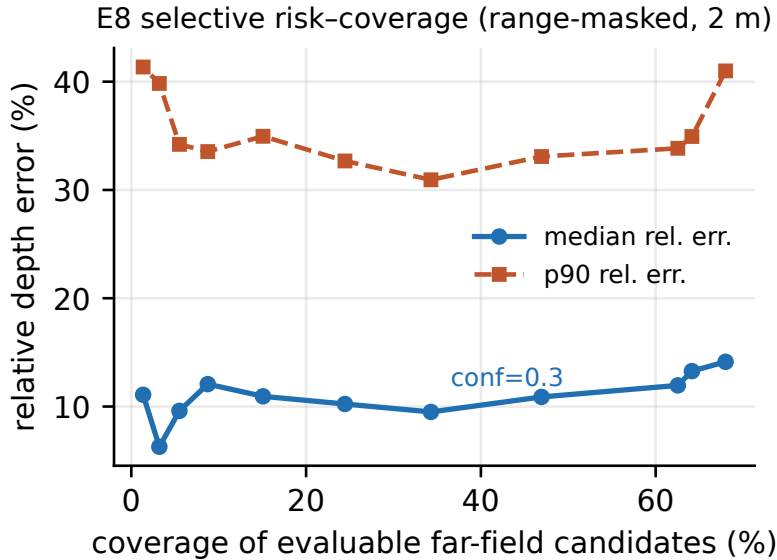


Figure 3: Selective risk-coverage on the controlled far-field cohort. Increasing the threshold initially reduces median and tail error; the knee is near confidence 0.3, after which stricter selection no longer improves error monotonically.

Real holes are harder than masked ones. When we instead score the *true* low-res LiDAR drop-outs (260 stable GT points after strict filtering), gated DH-Active covers 53.5% at 42.4% median error and 47.2% p90 error (all scene medians). Without gates the corresponding values are 58.9%, 46.4%, and 71.8%. Real drop-outs co-occur with edges, reflections, and occlusion, and are harder than a clean range mask; one of the five sequences has no gated output on its 12 surviving real-hole candidates. We therefore do *not* claim high-precision recovery of real holes, and the 6.7% random-hold-out number (§6.3) must not be read as a real-hole error. The cutoff sweep (Table 5) places the range-masked scene-median error between 11.3 and 13.4% across 1.5–2.5 m.

Table 5: Cutoff sensitivity (range-masked cohort, gated DH-Active). Controlled far-field error is stable across thresholds; 2 m balances sample count and PnP success.

cutoff	PnP success	candidates	coverage	median rel.
1.5 m	69.6%	113,556	66.5%	11.3%
2.0 m	89.2%	32,690	64.2%	13.4%
2.5 m	91.6%	7,254	71.9%	12.9%

6.5 Effect of the gate

On ARKitScenes we ablate the two gates while sweeping the keyframe gap. Removing the parallax gate has a severe effect—correlation falls from 0.745 to 0.034—whereas removing the reprojection gate is mild (0.745 \rightarrow 0.724). Across 16–60-frame gaps the relative error stays within 6.3–7.1% while coverage and correlation trade off against parallax. The parallax gate is thus the core safety mechanism: it is what implements abstention, directly supporting the design of §3.3.

Table 6: Gate ablation on ARKitScenes (scene-median). The parallax gate is essential.

configuration	corr	median rel. err.
gap 16	0.803	7.1%
gap 30 (default)	0.745	6.7%
gap 60	0.731	6.3%
parallax gate OFF (gap 30)	0.034	7.2%
reprojection gate OFF (gap 30)	0.724	6.8%

6.6 Comparison to learning-based multi-view geometry

We run DUST3R [29] and VGGT-1B [28] on the same five ARKitScenes sequences. The input conditions are *not* equal and we state this plainly: the learned baselines are RGB-only and receive a *per-frame ground-truth oracle scale* (fit on a disjoint pixel set), whereas DH-Active is LiDAR-anchored and metric with *no* scale alignment.

Table 7: Reference results on ARKitScenes under different inputs and scale protocols. The learned baselines receive per-frame ground-truth oracle scale; DH-Active receives sparse LiDAR and no post-hoc scale alignment. These are contextual measurements, not a head-to-head ranking.

method	median rel.	corr	GT scale?	metric?	compute
DH-Active	6.7%	0.745	no	yes	0-param, CPU real-time
DUST3R	7.2%	0.802	oracle	no	571 M, GPU, 78 s/vid
VGGT-1B	2.5%	0.967	oracle	no	1.26 B, GPU, 235 s/vid

VGGT-1B is clearly the most accurate after scale alignment. DUST3R’s median error is numerically close to DH-Active, but the inputs, output density, and scale treatment differ, so no equivalence or superiority follows from that proximity. Among the three implementations evaluated here, DH-Active is the one that emits metric depth without post-hoc alignment, with explicit abstention and zero learned parameters.

6.7 Downstream behaviour as a visual front-end

Finally we place the geometry features in two downstream proxy regressions. On RH20T (799 tasks, \sim 100k samples, task-hold-out, ridge probe over a shared robot-context baseline), future end-effector-motion regression with DH-Active features has validation MSE within 0.6–1.3% of DINOv2-L (ratio 1.006 over all samples and 1.013 on moving samples). This is a descriptive difference; we did not run an equivalence or non-inferiority test. On a single-scene visual-odometry proxy, DH-Active gives validation MSE 1.32 versus 1.63 for DINOv2 (ratio 0.81). The latter is a geometry-favoured, single-scene result, and the broader proxy is only weakly visual: every front end improves on context alone by 0.6–2.4%, and DH-Active does not beat raw RGB at scale. These experiments show that the features can be consumed by the probes at similar error, not that they preserve policy performance or improve action. That question requires a visually demanding task and a closed-loop evaluation.

7 Limitations

Our claims are bounded, by design. **No robot in the loop:** all downstream evidence is offline regression, never a task success rate; the RH20T comparison is descriptive and includes no equivalence test. **Scoped latency:** the 1.11 ms measurement covers the core single-frame stages, not tracking, PnP, triangulation, or preprocessing. **Map fragmentation:** sparse single-view spiral structure does not close into a room; triangulation widens coverage but does not stitch fragments, an orthogonal problem we do not solve. **Motion dependence:** recovery scales with translational baseline; nearly static hand-held clips give too little parallax and the gate (correctly) abstains. **Public data is harder:** on ARKitScenes only 1/5 sequences pass the strict correlation line, even as relative error stays \sim 5–9%; we do not claim iPhone-LiDAR generalisation from structured-light TUM. **Selective, not calibrated:** ECE is \sim 0.22–0.28 and the risk–coverage curve is not

strictly monotone; the score ranks but is not a probability. **Real holes:** the most direct measurement (§6.4) puts real-hole recovery at 42.4% median error on a small 260-point GT set, with one sequence yielding no gated output. This is not a precision-depth result. We state these limits so that no number in this paper is read beyond what it supports.

8 Conclusion

We presented DH-Active, a training-free geometry back-end that treats a short-range LiDAR not as the sole depth source but as a metric ruler: near returns anchor the two-view pose, that pose triangulates the far field, and a parallax/reprojection gate abstains where the geometry is weak, attaching a selective confidence to what remains. Under a strict controlled-cutoff protocol with independent laser ground truth, the method reaches 64.2% scene-median coverage of evaluable spiral-sampled far-field candidates at 13.4% scene-median relative error using only sub-2m returns; direct triangulation from the device trajectory is not usable. Its measured core front end runs in 1.11 ms on CPU with zero learned parameters. It does not match a billion-parameter learned model after oracle scale alignment, nor is that its aim. Alongside the positive results, we report the falsified alternatives—defocus, focus stacks, fusion, ICP-over-good-VIO, attention-to-holes—because they draw the boundary of where this honest, lightweight geometry is the right tool. We hope both halves are useful to anyone building edge perception that must say not only what it sees, but where it cannot see.

Reproducibility. Complete source, unit tests, and per-experiment configuration/result logs are prepared for public release alongside the paper. Public datasets are obtained from their official sources; no data or third-party weights are redistributed.

References

- [1] Gilad Baruch, Zhuoyuan Chen, Afshin Dehghan, Tal Dimry, Yuri Feigin, Peter Fu, Thomas Gebauer, Brandon Joffe, Daniel Kurz, Arik Schwartz, and Elad Shulman. ARKitScenes: A diverse real-world dataset for 3D indoor scene understanding using mobile RGB-D data. In *Advances in Neural Information Processing Systems (NeurIPS) Datasets and Benchmarks Track*, 2021.
- [2] Carlos Campos, Richard Elvira, Juan J Gómez Rodríguez, José M M Montiel, and Juan D Tardós. ORB-SLAM3: An accurate open-source library for visual, visual-inertial, and multimap SLAM. *IEEE Transactions on Robotics*, 37(6):1874–1890, 2021.
- [3] Robert L Cook. Stochastic sampling in computer graphics. *ACM Transactions on Graphics*, 5(1):51–72, 1986.
- [4] Brian Curless and Marc Levoy. A volumetric method for building complex models from range images. In *Proceedings of SIGGRAPH*, pages 303–312, 1996.
- [5] Ran El-Yaniv and Yair Wiener. On the foundations of noise-free selective classification. *Journal of Machine Learning Research*, 11:1605–1641, 2010.
- [6] Hao-Shu Fang, Hongjie Fang, Zhenyu Tang, Jirong Liu, Chenxi Wang, Junbo Wang, Haoyi Zhu, and Cewu Lu. RH20T: A comprehensive robotic dataset for learning diverse skills in one-shot. In *2024 IEEE International Conference on Robotics and Automation (ICRA)*, pages 653–660, 2024. doi: 10.1109/ICRA57147.2024.10611615.
- [7] Martin A Fischler and Robert C Bolles. Random sample consensus: a paradigm for model fitting with applications to image analysis and automated cartography. *Communications of the ACM*, 24(6):381–395, 1981.
- [8] Yonatan Geifman and Ran El-Yaniv. Selective classification for deep neural networks. In *Advances in Neural Information Processing Systems (NeurIPS)*, pages 4878–4887, 2017.
- [9] Chuan Guo, Geoff Pleiss, Yu Sun, and Kilian Q Weinberger. On calibration of modern neural networks. In *International Conference on Machine Learning (ICML)*, pages 1321–1330, 2017.
- [10] Richard Hartley and Andrew Zisserman. *Multiple View Geometry in Computer Vision*. Cambridge University Press, 2 edition, 2004.
- [11] Caner Hazirbas, Sebastian Georg Soyer, Maximilian Christian Staab, Laura Leal-Taixé, and Daniel Cremers. Deep depth from focus. In *Asian Conference on Computer Vision (ACCV)*, pages 525–541, 2018.
- [12] Hakyong Kim, Ruicheng Wang, Chengtang Yao, Jiaolong Yang, and Min H. Kim. Dense metric depth completion from sparse direct time-of-flight sensors. In *IEEE/CVF Conference on Computer Vision and Pattern Recognition (CVPR)*, pages 36518–36528, 2026.

- [13] Moo Jin Kim, Karl Pertsch, Siddharth Karamcheti, Ted Xiao, Ashwin Balakrishna, Suraj Nair, Rafael Rafailov, Ethan P. Foster, Pannag R. Sanketi, Quan Vuong, Thomas Kollar, Benjamin Burchfiel, Russ Tedrake, Dorsa Sadigh, Sergey Levine, Percy Liang, and Chelsea Finn. OpenVLA: An open-source vision-language-action model. In *Proceedings of the 8th Conference on Robot Learning*, volume 270 of *Proceedings of Machine Learning Research*, pages 2679–2713. PMLR, 2025.
- [14] Vincent Lepetit, Francesc Moreno-Noguer, and Pascal Fua. EPnP: An accurate $O(n)$ solution to the PnP problem. *International Journal of Computer Vision*, 81(2):155–166, 2009.
- [15] Bruce D Lucas and Takeo Kanade. An iterative image registration technique with an application to stereo vision. In *International Joint Conference on Artificial Intelligence (IJCAI)*, pages 674–679, 1981.
- [16] Maxim Maximov, Kevin Galim, and Laura Leal-Taixé. Focus on defocus: Bridging the synthetic to real domain gap for depth estimation. In *IEEE/CVF Conference on Computer Vision and Pattern Recognition (CVPR)*, pages 1071–1080, 2020.
- [17] Richard A Newcombe, Shahram Izadi, Otmar Hilliges, David Molyneaux, David Kim, Andrew J Davison, Pushmeet Kohli, Jamie Shotton, Steve Hodges, and Andrew Fitzgibbon. KinectFusion: Real-time dense surface mapping and tracking. In *IEEE International Symposium on Mixed and Augmented Reality (ISMAR)*, pages 127–136, 2011.
- [18] Maxime Oquab, Timothée Darcet, Théo Moutakanni, Huy Vo, Marc Szafraniec, Vasil Khalidov, Pierre Fernandez, Daniel Haziza, Francisco Massa, Alaaeldin El-Nouby, et al. DINOv2: Learning robust visual features without supervision. *Transactions on Machine Learning Research (TMLR)*, 2024.
- [19] Said Pertuz, Domenec Puig, and Miguel Angel Garcia. Analysis of focus measure operators for shape-from-focus. *Pattern Recognition*, 46(5):1415–1432, 2013.
- [20] Johannes L Schönberger and Jan-Michael Frahm. Structure-from-motion revisited. In *IEEE Conference on Computer Vision and Pattern Recognition (CVPR)*, pages 4104–4113, 2016.
- [21] Eric L Schwartz. Spatial mapping in the primate sensory projection: Analytic structure and relevance to perception. *Biological Cybernetics*, 25(4):181–194, 1977.
- [22] Jianbo Shi and Carlo Tomasi. Good features to track. In *IEEE Conference on Computer Vision and Pattern Recognition (CVPR)*, pages 593–600, 1994.
- [23] Hans Strasburger, Ingo Rentschler, and Martin Jüttner. Peripheral vision and pattern recognition: A review. *Journal of Vision*, 11(5):13, 2011.
- [24] Jürgen Sturm, Nikolas Engelhard, Felix Endres, Wolfram Burgard, and Daniel Cremers. A benchmark for the evaluation of RGB-D SLAM systems. In *IEEE/RSJ International Conference on Intelligent Robots and Systems (IROS)*, pages 573–580, 2012.
- [25] Qihao Sun, Jiarun Liu, Ziqian Ni, Jianyun Xu, Sheng Yang, Tao Xie, Lijun Zhao, and Ruifeng Li. LiDAR prompted spatio-temporal multi-view stereo for autonomous driving. In *IEEE/CVF Conference on Computer Vision and Pattern Recognition (CVPR)*, pages 14567–14577, 2026.
- [26] V. Javier Traver and Alexandre Bernardino. A review of log-polar imaging for visual perception in robotics. *Robotics and Autonomous Systems*, 58(4):378–398, 2010.
- [27] Helmut Vogel. A better way to construct the sunflower head. *Mathematical Biosciences*, 44(3-4):179–189, 1979.
- [28] Jianyuan Wang, Minghao Chen, Nikita Karaev, Andrea Vedaldi, Christian Rupprecht, and David Novotny. VGGT: Visual geometry grounded transformer. In *Proceedings of the IEEE/CVF Conference on Computer Vision and Pattern Recognition (CVPR)*, pages 5294–5306, 2025.
- [29] Shuzhe Wang, Vincent Leroy, Yohann Cabon, Boris Chidlovskii, and Jérôme Revaud. DUS3R: Geometric 3D vision made easy. In *IEEE/CVF Conference on Computer Vision and Pattern Recognition (CVPR)*, pages 20697–20709, 2024.
- [30] Alex Wong, Xiaohan Fei, Stephanie Tsuei, and Stefano Soatto. Unsupervised depth completion from visual inertial odometry. *IEEE Robotics and Automation Letters*, 5(2):1899–1906, 2020. doi: 10.1109/LRA.2020.2969938.
- [31] Yinda Zhang and Thomas Funkhouser. Deep depth completion of a single RGB-D image. In *IEEE/CVF Conference on Computer Vision and Pattern Recognition (CVPR)*, pages 175–185, 2018.